p-Type $BiVO_4$ for Solar O_2 Reduction to H_2O_2

Daye Seo,[1,†] Vrindaa Somjit,[2,†] Dae Han Wi,[1] Giulia Galli,[2,3,4,*] and Kyoung-Shin Choi[1,*]

[1]*Department of Chemistry, University of Wisconsin-Madison, Madison, WI 53706, United States*
[2]*Materials Science Division, Argonne National Laboratory, Lemont, IL 60439, USA*
[3]*Pritzker School of Molecular Engineering, University of Chicago, Chicago, IL 60637, USA*
[4]*Department of Chemistry, University of Chicago, Chicago, IL 60637, USA*

[†] These authors contributed equally to this work.

* Correspondence and requests for materials should be addressed to G.G. (email: gagalli@uchicago.edu) and K.-S.C. (email: kschoi@chem.wisc.edu).

Abstract

Photoelectrochemical cells (PECs) can directly utilize solar energy to drive chemical reactions to produce fuels and chemicals. Oxide-based photoelectrodes in general exhibit enhanced stability against photocorrosion, which is a critical advantage for building a sustainable PEC. However, most oxide-based semiconductors are n-type, and p-type oxides that can be used as photocathodes are limited. In this study, we report the synthesis, characterization, and application of p-type $BiVO_4$ with a monoclinic scheelite (*ms*) structure. *ms*-$BiVO_4$ is inherently n-type, and it has been investigated only as a photoanode to date. In this study, we prepared p-type *ms*-$BiVO_4$ (bandgap of 2.4 eV) via atomic doping of Ca^{2+} at the Bi^{3+} site under an O_2-rich environment and examined its performance as a photocathode. We then demonstrated that the Ca-doped *ms*-$BiVO_4$ photocathode can be used for solar O_2 reduction to H_2O_2 when coupled with appropriate catalysts. Our computational investigation using hybrid density functional theory revealed that holes are stable as polarons in *ms*-$BiVO_4$ and have a low self-trapping energy, that may lead to free carriers in the valence band at finite temperature. Our calculations also show that Ca is an effective shallow acceptor dopant with low formation energy and thermal ionization energy leading to p-type conductivity. Our joint experimental and computational results provide critical insights into the design of p-type *ms*-$BiVO_4$, enabling its use as a polaronic oxide photocathode.

Introduction

The use of a photoelectrochemical cell (PEC) can offer an energy-efficient synthesis route to fuels and value-added chemicals, as the solar energy harvested by photoelectrodes decrease or eliminate the energy input needed to drive the overall reaction by an electrochemical cell.[1,2] The photoelectrodes utilized in photoelectrochemical cells can be either n-type semiconductors (i.e., photoanodes) for oxidation reactions or p-type semiconductors (i.e., photocathodes) for reduction reactions.[3] Developing stable, low-cost, and high-performance semiconductor electrodes is the key to enabling the practical operation of a PEC.

Among the various photoelectrodes, oxide-based photoelectrodes have the advantage of being more robust in aqueous media. Also, they are easy to fabricate, and their compositions can be tuned easily to enhance desired properties.[4,5] Most oxide-based semiconductors are n-type due to oxygen vacancies serving as their intrinsic donor-type defects. As a result, most oxide-based photoelectrodes studied to date are photoanodes, and the realization of oxide-based photocathodes has been very limited.

The oxide-based photocathodes can be categorized into two major types: Cu-based photocathodes and Fe-based photocathodes.[5] The former (e.g., Cu_2O, CuO) generally suffer from photocorrosion while their electron-hole separation yields are relatively high. For example, p-type Cu_2O has generated the highest photocurrent among all oxide-based photocathodes for solar hydrogen production, but it requires protection and buffer layers to suppress photocorrosion.[6] On the other hand, Fe-based photocathodes (e.g., $LaFeO_3$, $Ca_2Fe_2O_5$, $BiFeO_3$) generally suffer from poor electron-hole separation while being more stable against photocorrosion.[7–10]

In our attempts to develop new oxide-based photocathodes beyond Cu-based and Fe-based systems, we considered the possibility of producing p-type $BiVO_4$. Monoclinic scheelite (*ms*) $BiVO_4$ is an n-type semiconductor with a bandgap of 2.4 eV that can achieve the highest electron-hole separation yield amongst all oxide-based photoanodes.[11] Furthermore, its operation for more than hundreds of hours has been demonstrated for solar water oxidation when it is paired with a proper oxygen evolution catalyst in an optimal electrolyte.[12,13] Thus, if *ms*-$BiVO_4$ can be doped as p-type, it may be able to generate higher photocurrent than Fe-based photocathodes while being more stable than Cu-based photocathodes.

We note that while p-type $BiVO_4$ materials have been reported previously, they are not *ms*-$BiVO_4$ but $BiVO_4$ with a tetragonal zircon (*tz*) structure that has a bandgap of 2.85 eV.[14,15] As *tz*-$BiVO_4$ cannot utilize visible light, we were specifically interested in making p-type *ms*-$BiVO_4$ that has a much smaller bandgap (~2.4 eV). It has been theoretically predicted that alkali (Na and K) and alkaline earth metal (Ca and Sr) ions substitutionally doped at the Bi sites in *ms*-$BiVO_4$ can serve as acceptor-type dopants.[16] However, all the experimentally prepared Ca-doped *ms*-$BiVO_4$ photoelectrodes reported to date showed only n-type behavior.[17,18] Among these studies, the work by Abdi and co-workers reported that they produced p-type Ca-doped *ms*-$BiVO_4$.[17] However, Ca-doped *ms*-$BiVO_4$ in this study was formed as part of n-type *ms*-$BiVO_4$ by gradient Ca doping and not as an isolated p-type material, and the presence of the Ca-doped *ms*-$BiVO_4$ layer resulted in the enhancement of the *anodic* photocurrent of underlying n-type *ms*-$BiVO_4$. Thus, the synthesis of p-type Ca-doped *ms*-$BiVO_4$ that produces *cathodic* photocurrent and enables the investigation and application of p-type *ms*-$BiVO_4$ as a photocathode has yet to be shown.

In this study, we report a critical Ca doping condition resulting in the formation of p-type *ms*-$BiVO_4$ that generates cathodic photocurrent. The photocurrent generated by the Ca-doped *ms*-$BiVO_4$ is higher than those generated by Fe-based photocathodes. Also, the Ca-doped $BiVO_4$ is

much more stable than Cu-based photocathodes. After characterizing the p-type behavior of Ca-doped *ms*-$BiVO_4$, we demonstrate its use for solar O_2 reduction to H_2O_2, a highly valuable chemical used for various industrial bleaching processes as well as chemical synthesis.[19] We also computationally investigated the formation and behavior of hole polarons in *ms*-$BiVO_4$ using hybrid density functional theory. Moreover, we examined the formation energy and thermal ionization of Ca as an acceptor dopant. By examining the characteristics and energetics of both free hole polarons and hole polarons specifically generated from the Ca acceptor dopant in *ms*-$BiVO_4$, our study provides important understanding of the formation and behavior of p-type *ms*-$BiVO_4$ for use as a photocathode.

Experimental

Materials. Bismuth(III) nitrate pentahydrate ($Bi(NO_3)_3 \cdot 5H_2O$, 98%), potassium iodide (KI, 99+%), nitric acid (HNO_3, 70%), *p*-benzoquinone (*p*-BQ, >98%), vanadium acetylacetonate ($VO(C_5H_7O_2)_2$, 98%), calcium nitrate tetrahydrate ($Ca(NO_3)_2 \cdot 4H_2O$, >99%), dimethyl sulfoxide (DMSO, 99.9%), potassium hydroxide (KOH, >85%), potassium sulfate (K_2SO_4), sodium acetate, acetic acid, potassium nitrate (KNO_3, >99.0%), potassium tetrachloroplatinate(II) (K_2PtCl_4, 98%) hydrogen peroxide (H_2O_2, 30% (w/w) in H_2O, contains stabilizer) were purchased from Sigma-Aldrich. Lactic acid (85%) and silver(I) nitrate ($AgNO_3$, 99.9+%) were purchased from Alfa-Aesar Chemicals. Ethanol (200 proof) was purchased from Decon Laboratories, and tetrabutylammonium hexafluorophosphate ($TBAPF_6$, >98%) was purchased from TCI Chemicals. The deionized water (DI water, >18 MΩ·cm) used in this study was prepared by the Barnstead E-pure water purification system. All chemicals were used as purchased without further purification. Glass substrates coated with fluorine-doped tin oxide (FTO) were purchased from Hartford Glass Co. Nafion membranes (N211) were purchased from Fuel Cell Store.

Preparation of $BiVO_4$ electrodes. Pristine n-type *ms*-$BiVO_4$ and Ca-doped $BiVO_4$ electrodes were prepared using the same Bi precursor, BiOI film, but with different dropcasting and annealing conditions (**Figure 1**). BiOI films were electrodeposited using a previously reported method briefly described here.[12] The plating solution was prepared by mixing four different solutions: 1) 50 mL of an aqueous solution containing 15 mM $Bi(NO_3)_3$ and 400 mM KI, 2) 20 mL of ethanol solution containing 46 mM of *p*-BQ, 3) 169 µL of lactic acid (85%), and 4) 120 µL of 10-fold-diluted concentrated nitric acid. Prior to use, FTO electrodes were cleaned by sonicating in soapy water and isopropanol successively. After dried under a stream of air, the FTO electrodes were masked with PTFE tape such that the exposed area was 1 cm x 1.25 cm. A typical 3-electrode system with an FTO working electrode, an FTO counter electrode, and an Ag/AgCl (4 M KCl) reference electrode was employed. We used FTO as the working electrode because it is stable under the annealing conditions used to produce $BiVO_4$, and its transparency allows for back-side illumination; for both n-type and p-type $BiVO_4$, back-side illumination results in better performances than front-side illumination. The electrodeposition of BiOI was performed by sequentially applying two different potentials: 1) –0.33 V (vs. Ag/AgCl (4 M KCl)) for 20 s to induce Bi nucleation and 2) –0.1 V (vs. Ag/AgCl (4 M KCl)) for BiOI growth. The charge passed during the growth step was 0.32 C/cm^2. As-deposited films were washed with DI water and dried under a stream of air.

In order to convert the BiOI films into pristine n-type $BiVO_4$, 75 μL of a DMSO solution containing 200 mM $VO(C_5H_7O_2)_2$ was dropcast onto the BiOI film, and then the film was annealed at 450 °C for 2 h (ramping rate: 2 °C/min) in air. On the other hand, to convert BiOI into Ca-doped $BiVO_4$, the dropcasting solution was prepared by adding 20 μL of an aqueous solution containing 100 mM $Ca(NO_3)_2$ into 2 mL of a DMSO solution containing 150 mM $VO(C_5H_7O_2)_2$, and then 75 μL of it was dropcast onto the BiOI films. The concentration of Ca^{2+} in the dropcasting solution was 1 mM, which was found to be the optimal concentration. Increasing the Ca^{2+} concentration to 2 mM or decreasing it below 0.5 mM reduced photocurrent generation (**Figure S1**). The annealing condition for Ca-doped $BiVO_4$ was 2 h at 550 °C while flowing O_2 (ramping rate: 4.5 °C/min, O_2 flowing rate: 75 ccm). Excess V_2O_5 was removed by soaking the electrodes in a 0.85 M KOH solution for 30 min, and then, any Ca residues such as $Ca(OH)_2$ or CaO were removed by soaking the electrode in a 0.5 M K_2SO_4 solution (pH 2) for another 30 min.

Materials characterization. The surface morphology and elemental composition of the pristine and Ca-doped $BiVO_4$ films were determined by scanning electron microscopy (SEM; Leo Supra55 VP, accelerating voltage 2 kV) and an energy dispersive X-ray spectroscopy (EDS; Noran System Seven, Thermo-Fisher, ultra-dry silicon drift detector, accelerating voltage: 22 kV), respectively. The purity and crystallinity of the films were characterized by X-ray diffraction (XRD; D8 Discover, Bruker, Ni-filtered Cu Kα radiation, λ = 1.5418 Å). Bandgaps were determined from UV–visible (UV–vis) absorption spectra obtained using an integrating sphere to collect all reflected and transmitted light, allowing for a more accurate determination of absorbance (Cary 5000 UV–vis–NIR spectrophotometer, Agilent). An X-ray photoelectron spectrometer (XPS, K-Alpha X-ray Photoelectron Spectrometer, Thermo Scientific) with Al Kα X-ray source was used to confirm the existence of Ca in Ca-doped $BiVO_4$ and examine the atomic ratio of Pt: Ag in the Pt/Ag electrocatalyst used for photoelectrochemical O_2 reduction. The high-angle annular dark-field–scanning transmission electron microscope (HAADF–STEM) and corresponding EDS elemental mapping images of Pt/Ag catalysts on $BiVO_4$ were collected using a field emission transmission electron microscope (FEI Tecnai TF 30) operated at 300 kV. To prepare the STEM sample, Pt/Ag loaded $BiVO_4$ powder was collected by scratching the surface of the photoanode and dispersed in ethanol. Then, 2.5 μL of the colloidal solution was placed multiple times on a lacey carbon-supported 400 mesh Cu grid (Electron Microscopy Sciences).

Photoelectrochemical and electrochemical characterization. All photoelectrochemical and electrochemical measurements were conducted with an SP-200 potentiostat/EIS (Bio-Logic Science Instrument). Solar illumination was simulated by filtering light from a 300-W Xe arc lamp through the following successive filters: water IR filter, neutral density filters, and an AM 1.5 G filter. The light was collimated and directed onto the sample via an optical fiber, and the light was calibrated to 100 mW/cm^2 (1 sun) using an NREL-certified GaAs reference cell (PV Measurements). The photoelectrode was illuminated through the glass side first (back-side illumination), and the illuminated area was 0.06 cm^2. A typical 3-electrode setup with a $BiVO_4$ working electrode, a graphite rod counter electrode, and an Ag/AgCl (4 M KCl) reference electrode was used in an undivided cell.

The photocurrent density–potential (*J–V*) plots of $BiVO_4$ electrodes were obtained in a 0.5 M sodium acetate buffer solution (pH 4.3) with *p*-BQ (10 mM) as an electron scavenger. The *J–V* plots were obtained under chopped illumination to measure the dark current and photocurrent densities during a single potential scan. The potential was scanned from the open circuit potential

(ocp) to the negative direction with a scan rate of 5 mV/s for Ca-doped $BiVO_4$ photocathodes. When the photoelectrodes showed only anodic photocurrents, the potential was scanned from ocp to the positive direction to make the comparison between the photocathodes and the photoanodes clearer.

All results in this work are presented with respect to the reversible hydrogen electrode (RHE) for easy comparison with other reports using various pH conditions unless otherwise specified. Potentials vs. Ag/AgCl (4 M KCl) reference electrodes were converted to potentials vs. RHE using Eq. 1.

$$E_{(\text{vs. RHE})} = E_{(\text{vs. Ag/AgCl})} + E_{\text{Ag/AgCl (4 M KCl)}} + (0.0591\ \text{V} \times \text{pH}) \quad (1)$$
where $E_{\text{Ag/AgCl (4 M KCl)}} = 0.1976$ V vs. NHE at 25 °C

Wavelength-dependent photocurrents of Ca-doped $BiVO_4$ were measured using the same electrolyte condition with the same 3-electrode configuration used in the above experiment. The light source was a 150 W Xe arc lamp equipped with an AM 1.5G filter and neutral density filters, and monochromatic light was generated by an Oriel Cornerstone 130 monochromator with a 10 nm interval. The power of light at each wavelength was measured by a Si photodiode (SED 033, International Light Technologies). The photocurrent was measured while applying a constant potential (0.6 V) in a homemade Faraday cage. Based on the measured photocurrents, the incident photon-to-current efficiency (IPCE) was determined using Eq. 2.

$$\text{IPCE}(\%) = \frac{1240\ (\text{eV nm}) \times \left|\text{Photocurrent density (mA/cm}^2)\right|}{\text{Incident light power density (mW/cm}^2) \times \text{Wavelength (nm)}} \times 100(\%) \quad (2)$$

Photoelectrochemical H_2O_2 production. Three different electrocatalysts were placed on Ca-doped $BiVO_4$ and examined for the reduction of O_2 to H_2O_2: Pt, Ag, and Pt covered with Ag (referred to as Pt/Ag). These electrocatalysts were photoelectrochemically deposited onto the $BiVO_4$ photocathodes using a 3-electrode configuration with a $BiVO_4$ photocathode working electrode, an FTO counter electrode, and a Ag/AgCl (4 M KCl) or Ag/Ag^+ (10 mM $AgNO_3$) reference electrode under AM 1.5G illumination. Simulated solar light was generated using an LCS-100 solar simulator (Oriel Instruments) equipped with a 100W Xe arc lamp (Newport) and an AM 1.5G filter. An infrared filter (Newport) and a focusing lens were placed between the light source and the photoelectrode. As back-side illumination was used, the light intensity was calibrated to 100 mW/cm^2 at the back side of the photoelectrode using the GaAs reference cell. The entire area of the Ca-doped $BiVO_4$ electrode (~1.25 cm^2) was illuminated.

Pt was deposited at 0.3 V vs. Ag/AgCl in an aqueous solution containing 0.5 mM K_2PtCl_4 and 0.1 M KNO_3 by passing 6 mC/cm^2. Ag was deposited in a DMSO solution containing 1 mM $AgNO_3$ and 0.1 M $TBAPF_6$ at 0 V vs. Ag/Ag^+ by passing 3 mC/cm^2. Pt/Ag was deposited by first depositing Pt and then Ag using the same conditions used to deposit individual catalysts.

Photoelectrochemical H_2O_2 production was examined in O_2-purged 0.5 M K_2SO_4 solutions (pH 2 and pH 3) using the same illumination setup used for the photoelectrochemical electrocatalyst deposition. For the *J–V* plot measurement, the potential was scanned from the ocp to the negative direction with a scan rate of 5 mV/s under illumination and in the dark for comparison. For the quantitative analysis of H_2O_2, the photoelectrochemical O_2 reduction reaction (PORR) was performed at a constant potential of 0.8 V vs. RHE for 15 min in the same 0.5 M K_2SO_4 solution using a homemade quartz cell where cathodic and anodic chambers were divided by a Nafion membrane. The working (catalyst-deposited Ca-doped $BiVO_4$) and reference electrode

(Ag/AgCl (4 M KCl)) were immersed in the cathodic chamber, and the counter electrode (a graphite rod) was immersed in the anodic chamber. The solution in the cathodic chamber (20 mL) was purged with O_2 before and during the measurement.

For each of Ca-doped $BiVO_4$/Ag, Ca-doped $BiVO_4$/Pt, and Ca-doped $BiVO_4$/Pt/Ag, four measurements were made using four different samples to determine average performances with standard deviations. The amount of produced H_2O_2 for each electrolysis was quantified using iodometric titration, explained in the next paragraph. For a long-term stability test, the *J–t* plot measurement at 0.8 V vs. RHE was continued for 10 hours and the photoelectrode was examined by SEM and XRD after the *J–t* plot measurement.

For iodometric titration, 1 mL of the electrolyte used in photoelectrochemical O_2 reduction was taken and diluted with 1 mL of DI water. Then, 1 mL of a 0.4 M KI solution was added. In this solution, photoelectrochemically generated H_2O_2 reacts with I^- forming I_3^- which absorbs light between 250–500 nm. UV–vis absorption spectra were measured by a spectrophotometer (Cary 5000 UV–vis–NIR spectrophotometer, Agilent), and absorbance at 355 nm was used for the construction of the calibration curve (**Figure S2**) and the quantification of the amount of produced H_2O_2. Faradaic efficiency (FE) for H_2O_2 production was calculated by dividing the charges used to produce the detected amount of H_2O_2 by the total charge passed during the electrolysis using Eq. 3, where *n* is the number of electrons required to produce one H_2O_2 molecule, which is 2, and *F* is Faraday's constant (96485.33 C/mol).

$$\mathrm{FE}(\%) = \frac{n \times \text{amount of } H_2O_2 \text{ (mol)} \times F \text{ (C/mol)}}{\text{Total charge passed (C)}} \times 100(\%) \quad (3)$$

Computational Methods. Density functional theory (DFT) calculations within the Kohn-Sham framework[20,21] were carried out using the plane-wave pseudopotential method as implemented in the Quantum Espresso code.[22–24] We used ONCV pseudopotentials,[25,26] with the following valence electrons for Bi, V, O, and Ca: $5d^{10}6s^26p^3$, $3s^23p^64s^23d^3$, $2s^22p^6$, and $3s^23p^64s^2$ respectively, and a plane-wave cutoff of 60 Ry. Since the self-interaction error of semi-local functionals can be substantial, leading to an erroneous prediction of the delocalization of single particle electronic states,[27–29] we used the dielectric-dependent hybrid (DDH) functional for our calculations, to mitigate the self-interaction error. The Hartree-Fock mixing parameter α for the DDH functional was set to 0.145 ($\alpha = \varepsilon_\infty^{-1}$, where the high frequency dielectric constant ε_∞ = 6.9, as calculated using density functional perturbation theory in our previous study[30]). Calculations were carried out with a 4 × 4 × 2 supercell (768 total atoms with 128 Bi atoms) of monoclinic $BiVO_4$, using experimental lattice constants at 298 K (a = 5.1935 Å, b = 5.0898 Å, c = 11.6972 Å, α = 90°, β = 90°, γ = 90.3870°).[31] Such a large supercell was chosen to ensure defect concentrations relevant to our experiments (i.e., replacing one Bi atom with Ca atom resulting in Ca/(Bi+Ca) = 0.0078, compared to 0.015 in experiments). The fundamental bandgap obtained with the DDH functional, after accounting for renormalization effects (including spin-orbit coupling, finite temperature vibrations, and nuclear quantum effects, taken as 1.05 eV from Wiktor et al.[32] who used a PBE0-like functional), is 2.44 eV; this value is consistent with that obtained from photocurrent onset measurements (2.46 eV).[30] The Brillouin zone was sampled with the Γ point in all our calculations.

We investigated a single hole polaron and a Ca substitutional dopant on the Bi site. For the latter, we investigated both a neutral supercell and a supercell where we introduced an extra electron. All defect geometries were fully optimized with a force convergence threshold of 0.01 eV/Å, keeping the lattice parameters fixed.

We calculated the defect formation energies $E^f[(Ca_{Bi})^q]$ of the Ca substitutional dopant in the charge state q using Eq. 4,[33] where $E_{tot}[(Ca_{Bi})^q]$ is the total energy of the supercell containing the Ca dopant on the Bi site, $E_{tot}[bulk]$ is the total energy of the perfect crystal obtained using a supercell of the same size, μ_{Ca} is the chemical potential of Ca, μ_{Bi} is the chemical potential of Bi, ε_F is the Fermi energy relative to the valence band maximum (VBM), E_{VBM}, and E_{corr} is a charge-state dependent term that corrects for artificial electrostatic interactions arising due to the finite size of the periodic supercell[34] (using ϵ_0 = 52),[30] thus allowing for the extrapolation of computed defect properties to the dilute limit.

$$E^f[(Ca_{Bi})^q] = E_{tot}[(Ca_{Bi})^q] - E_{tot}[bulk] - \mu_{Ca} + \mu_{Bi} + q(\varepsilon_F + E_{VBM}) + E_{corr} \quad (4)$$

We calculated the polaron self-trapping energy $E_{self-trap}$ using Eq. 5,[35,36] where $E_{tot}[polaron]$ is the total energy of the supercell containing a hole which localizes to form a polaron, and $E_{tot}[delocalized]$ is the total energy of the pristine supercell with a hole that is delocalized. Hence $E_{self-trap}$ represents the energy gained in the formation of the hole polaron from a delocalized carrier in the valence band, and it is equivalent to the polaron binding energy. The magnitude of $E_{self-trap}$ is the energy required to excite the hole from its localized state to a delocalized state in the valence band.

$$E_{self-trap} = E_{tot}[polaron] - E_{tot}[delocalized] \quad (5)$$

Results and Discussion

Synthesis and characterization of Ca-doped $BiVO_4$. Both pristine and Ca-doped $BiVO_4$ were prepared using the same Bi precursor, electrochemically deposited BiOI films. The BiOI films are composed of vertically aligned BiOI sheets. As these sheets are thin and they grow with ample space between them, they serve as a precursor to form high surface area, nanoporous $BiVO_4$ films (**Figure 1**).[11] To convert the BiOI film into an n-type *ms*-$BiVO_4$ film (referred to as a pristine $BiVO_4$), a V-containing DMSO solution was dropcast onto BiOI, and then the film was annealed in air at 450 °C. In order to convert the BiOI film to Ca-doped *ms*-$BiVO_4$, a V-containing DMSO solution which also contains a small amount of $Ca(NO_3)_2$ was dropcast onto the BiOI film. The annealing condition was modified to 550 °C under O_2 conditions. The higher temperature was needed to incorporate Ca into the $BiVO_4$ lattice. The use of O_2 during annealing was found to be critical for producing p-type Ca-doped $BiVO_4$, as discussed in detail below. Excess V and Ca that did not incorporate into the $BiVO_4$ lattice were removed by base and acid treatments, respectively.

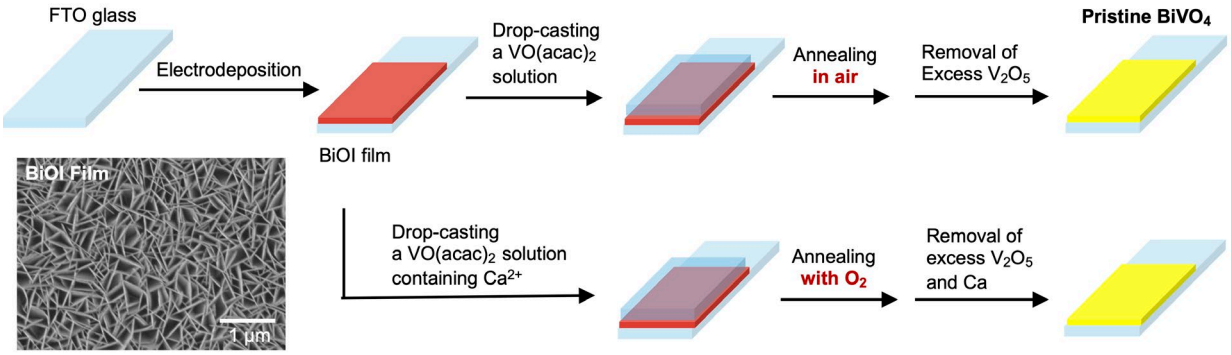

Figure 1. A scheme showing the synthesis procedure for pristine and Ca-doped $BiVO_4$. An SEM image of BiOI films used for $BiVO_4$ synthesis is also shown.

SEM images of pristine and Ca-doped $BiVO_4$ films show that they have similar nanoporous morphologies and uniform porosities throughout the films (**Figure 2**). The side-view SEM images show that the Ca-doped $BiVO_4$ film (~800 nm) is thinner than the pristine $BiVO_4$ film (~1.2 μm) although they were prepared using the same BiOI precursor films. This difference is due to the higher annealing temperature used for the synthesis of Ca-doped $BiVO_4$ facilitating grain growth, resulting in the contraction of the film.

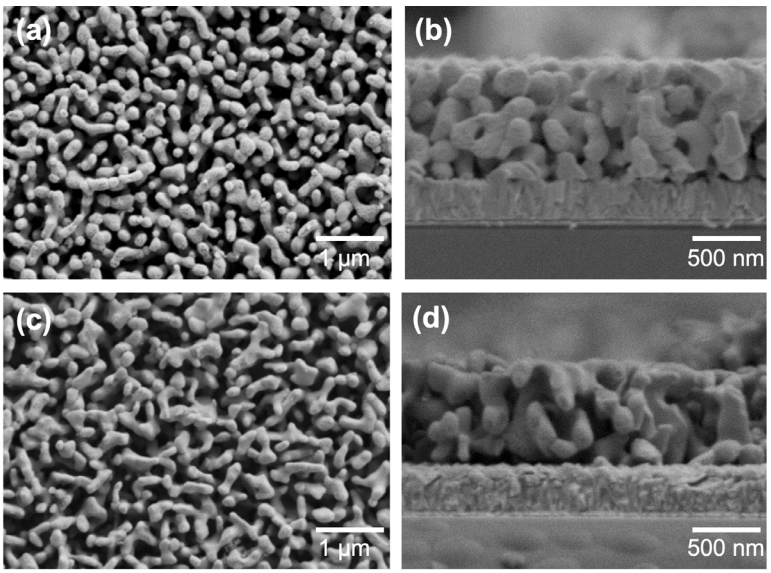

Figure 2. Top-view and side-view SEM images of (a,b) pristine $BiVO_4$ and (c,d) Ca-doped $BiVO_4$.

The presence of Ca in Ca-doped $BiVO_4$ was confirmed by EDS and XPS (**Figure S3**). The ionic radius of Ca^{2+} (1.12 Å) is comparable to that of B^{i3+} (1.17Å) while it is significantly bigger than that of V^{5+} (0.355 Å).[37] Considering the size and the coordination preference of Ca^{2+}, it is unlikely that Ca^{2+} can be stabilized in the four-coordinate, tetrahedral site of V. Thus, it is reasonable to think that Ca^{2+} is stabilized at the Bi^{3+} site. The amount of Ca^{2+} was varied and the optimal Ca^{2+} content was identified by measuring the photocurrent of resulting samples (**Figure**

S1). The atomic Bi:Ca ratio of the best performing sample measured by EDS was 98.5:1.5, and its empirical formula can be written as $Ca_{0.015}Bi_{0.985}VO_4$, meaning 1.5 at% of Bi^{3+} is replaced by Ca^{2+}. We will discuss only the results obtained from this best performing sample below.

The XRD patterns of pristine and Ca-doped $BiVO_4$ were compared in **Figure 3a**. They equally show peaks expected for crystalline *ms*-$BiVO_4$ with no apparent changes in cell parameters. No changes in cell parameters were expected considering the similar ionic sizes of Ca^{2+} and Bi^{3+} as well as the small amount of Ca^{2+} incorporated into the $BiVO_4$ lattice. However, upon Ca doping, some pairs of peaks became closer to each other (i.e., (110) and (011), (200) and (002), and (240) and (042) shown in **Figure 3b**). We note that the scheelite structure of $BiVO_4$ can be crystallized in both a tetragonal cell and a monoclinic cell.[31,38,39] Their structures are very similar; however, in the monoclinic cell, the coordination environments of Bi^{3+} were slightly distorted due to the expression of its $6s^2$ lone pair and this distortion removes the four-fold rotational axis necessary for a tetragonal symmetry. In the tetragonal cell with a higher symmetry, the aforementioned peak pairs merge into one peak.[39] Thus, the fact that the separation of these peak pairs is decreased by Ca doping means that the incorporation of Ca^{2+} into the Bi^{3+} site slightly reduces the average distortion at the Bi^{3+} site, as Ca^{2+} does not have a lone pair of electrons. In fact, these subtle changes in the XRD pattern of Ca-doped $BiVO_4$ are clear evidence that Ca^{2+} is truly incorporated into the crystal structure of *ms*-$BiVO_4$.

The UV–vis absorption spectra of pristine and Ca-doped $BiVO_4$ electrodes are shown in **Figure 3c**. The results show that Ca doping does not affect the bandgap or absorption coefficient of $BiVO_4$ considerably other than a slight red-shift of the bandgap. The bandgap of Ca-doped $BiVO_4$ was determined to be ~2.4 eV.

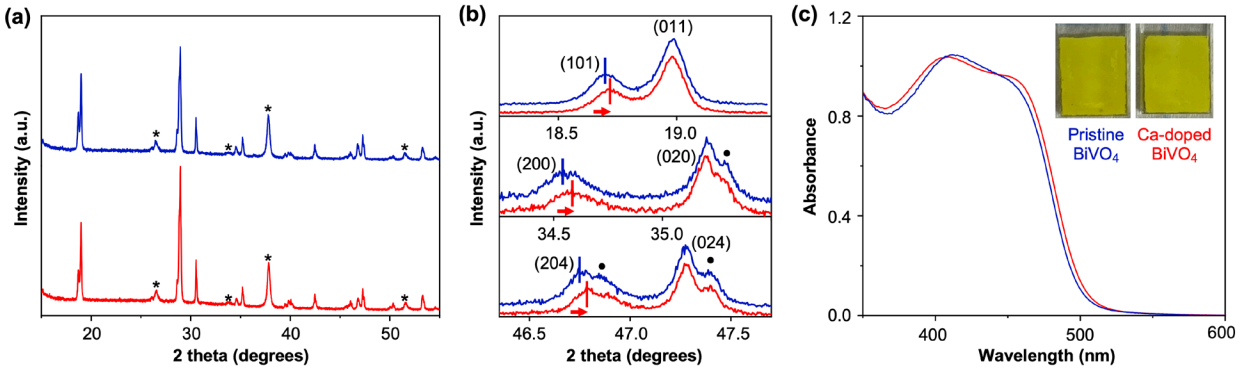

Figure 3. (a) XRD patterns of pristine (blue) and Ca-doped (red) $BiVO_4$. Peaks from the FTO substrate are marked with asterisks (*). (b) Magnification of a few selected (*hkl*) peak pairs to demonstrate the effect of Ca doping on their peak separation. Above 35 degrees, diffraction peaks from the Cu $K_{\alpha 2}$ source are separated from those from the Cu $K_{\alpha 1}$ source, and they are marked with •. (c) UV–vis absorption spectra of pristine (blue) and Ca-doped (red) $BiVO_4$. The insets are the photographs of the photoelectrodes.

P-type photoelectrochemical properties of Ca-doped $BiVO_4$. The photoelectrochemical property of Ca-doped $BiVO_4$ was first evaluated using *p*-BQ as an electron scavenger. The reduction potential of *p*-BQ to the corresponding hydroquinone is 0.699 V vs. RHE. As the conduction band minimum (CBM) of $BiVO_4$ is located close to 0.00 V RHE,[39] the photoexcited electrons at the CBM of Ca-doped $BiVO_4$ have sufficient overpotential to drive this reduction

reaction. Also, the kinetics of *p*-BQ reduction is faster than those of oxygen reduction or water reduction reactions. Thus, *p*-BQ can be used as an electron scavenger to preliminarily assess the type and magnitude of photocurrent that can be generated by Ca-doped $BiVO_4$ without adding any catalyst to help the interfacial electron transfer.

Figure 4a shows the *J–V* plot of Ca-doped $BiVO_4$ obtained in a 10 mM *p*-BQ solution (pH 4.3, acetate buffer) under AM 1.5G illumination (100 mW/cm^2). The light was chopped to obtain photocurrent and dark current in a single scan. When the light is on, Ca-doped $BiVO_4$ generates a cathodic photocurrent, confirming it is p-type. To the best of our knowledge, this is the first time that *ms*-$BiVO_4$ is prepared as a p-type semiconductor that can generate cathodic photocurrent under illumination.

The photocurrent onset potential is ~1.1 V vs. RHE, and this means that the flatband potential of Ca-doped $BiVO_4$ is ≥ ~1.1 V vs. RHE. (If *p*-BQ reduction is an ideal electron scavenger that completely suppresses surface electron-hole recombination, the photocurrent onset potential is the same as the flatband potential. Otherwise, the photocurrent onset appears at a potential less positive than the flatband potential.)[40] This value is more positive than the flatband potential of Cu_2O (e.g. < 0.8 V vs. RHE)[41] and is comparable to those of most Fe-based ternary oxide photocathodes such as $LaFeO_3$, $Ca_2Fe_2O_5$, and $BiFeO_3$.[7–10]

The IPCE measurement shows that it can utilize approximately 20% of incident photons with a wavelength shorter than 460 nm even when the applied bias is as positive as 0.65 V vs. RHE (**Figure 4b**). The photocurrent onset appears at 520 nm, which agrees well with the bandgap estimated from the UV–vis spectrum of Ca-doped $BiVO_4$.

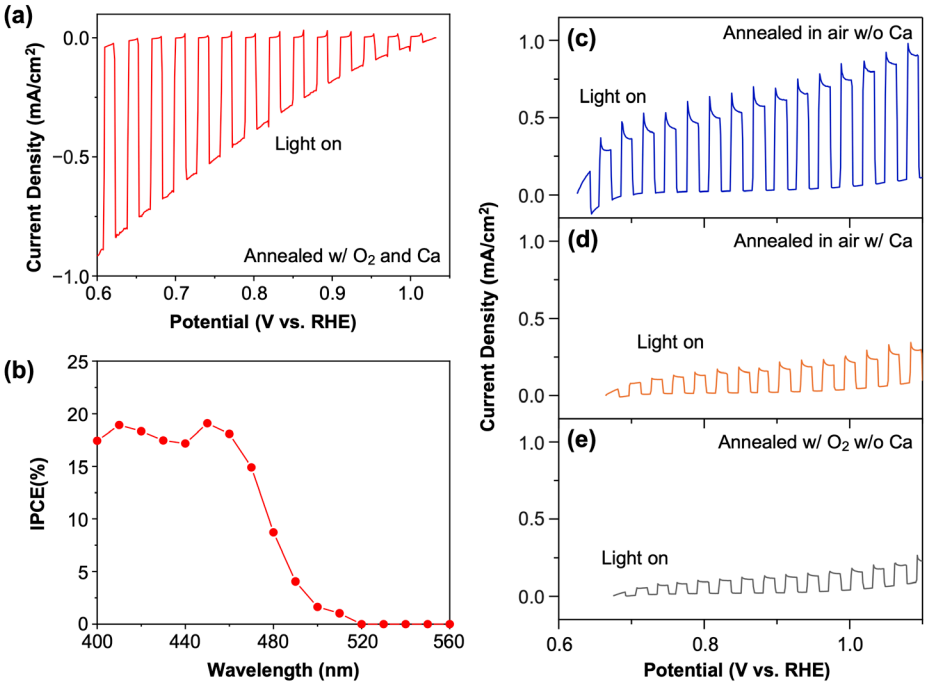

Figure 4. Photoelectrochemical properties of $BiVO_4$ electrodes. All measurements were conducted in a 0.1 M potassium acetate solution (pH 4.3) using *p*-BQ as an electron scavenger. *J–V* plots of (a) Ca-doped $BiVO_4$ and (c–e) control $BiVO_4$ photoelectrodes under chopped AM 1.5G illumination (100 mW/cm^2). Three control samples were prepared by conducting the thermal

treatment (c) in air without Ca (pristine), (d) in air with Ca, and (e) with O_2 and without Ca. (b) IPCE of Ca-doped $BiVO_4$ at 0.65 V vs. RHE.

When the *J–V* plot was obtained using pristine $BiVO_4$ under the same condition, anodic photocurrent was obtained when the light was on (**Figure 4c**), which was expected as pristine $BiVO_4$ is n-type. As the electrolyte did not contain any hole scavenger, the anodic photocurrent of pristine $BiVO_4$ was due to water oxidation. We also examined the photoelectrochemical properties of $BiVO_4$ samples prepared under different annealing conditions, which provided insights into the critical conditions required to produce p-type $BiVO_4$. For example, the Ca-doped $BiVO_4$ sample prepared by annealing in air (instead of with O_2) shows n-type behavior (**Figure 4d**). The careful XRD analysis of this sample shows that the separations of the aforementioned *hkl* peak pairs decrease, but their separations are less than those observed in the Ca-doped $BiVO_4$ sample prepared by annealing with O_2 (**Figure S4**). This result means that the amount of Ca incorporated without O_2 is less than that incorporated with O_2 and that the holes generated by Ca doping without O_2 are not sufficient to become the majority carrier. In order for holes to become the majority carrier, incorporating more Ca dopants (serving as acceptors) and decreasing O vacancies (serving as donors) are needed, and annealing with O_2 appears to promote both. This observation is well supported by the computational results discussed below. These results also explain one potential reason why previously reported Ca-doped $BiVO_4$ were n-type[17,18]; while they were made by different synthesis methods, they were commonly annealed in air.

$BiVO_4$ annealed under an O_2 environment but without Ca^{2+} also showed an anodic photocurrent (**Figure 4e**). This result means that reducing the amount of O vacancy is not enough to induce p-type behavior and incorporating an acceptor dopant like Ca^{2+} is critical for preparing p-type $BiVO_4$.

Photoelectrochemical H_2O_2 production with Ca-doped $BiVO_4$. Next, we examined the use of Ca-doped $BiVO_4$ photocathodes for photoelectrochemical O_2 reduction to H_2O_2. H_2O_2 is an important chemical used for various industrially and environmentally important oxidation processes, such as paper and pulp bleaching and the Fenton reaction used in wastewater treatment.[19,42] Currently, H_2O_2 is produced by the anthraquinone-based method, which is composed of complex and energy-intensive steps, including the consumption of H_2 for the reduction of anthraquinone. As a result, H_2O_2 production is centralized and the need to transport H_2O_2 to application locations creates additional cost and safety concerns.[19,43] Due to these reasons, 2-electron O_2 reduction reaction (ORR) to H_2O_2 has received much attention as a less energy-intensive and environmentally benign alternative method for H_2O_2 production, which may enable on-site H_2O_2 production.[19,44] PORR to H_2O_2 using a photocathode can be more energy efficient than electrochemical O_2 reduction reaction (EORR) to H_2O_2 owing to the photovoltage gained by the photocathode utilizing the solar energy.[10,45]

It is known that carbon-based electrocatalysts can achieve efficient and selective 2-electron ORR in basic solutions.[46] However, H_2O_2 is not stable in basic solutions for a prolonged time.[47,48] Also, some applications need H_2O_2 in acidic solutions (e.g., Fenton reaction at pH ~3).[42,49] Therefore, there is a great need to produce H_2O_2 in acidic solutions. Unfortunately, 2-electron ORR in acidic solutions is more difficult to achieve in terms of both selectivity and overpotential requirement.[49]

In this study, we used mildly acidic conditions (pH 2–3) to demonstrate 2-electron PORR by using a Ca-doped $BiVO_4$ photocathode. $BiVO_4$ is one of the few oxides that is chemically stable in mildly acidic solutions. However, we found that bare Ca-doped $BiVO_4$ generates negligible PORR in an O_2-purged 0.5 M K_2SO_4 solution (**Figure 5**, solid black). Thus, we deposited Pt/Ag nanoparticle catalysts on Ca-doped $BiVO_4$. Pt/Ag represents the Pt nanoparticle catalysts coated by Ag. Ag is known for its ability to promote 2-electron EORR in acidic solutions.[50] However, when we deposited Ag nanoparticle catalysts alone, while an impressive Faradaic efficiency (85.9±4.3%) for photoelectrochemical H_2O_2 production was achieved, the photocurrent density was very low (–0.11 mA/cm^2 at 0.8 V vs. RHE) compared to the photocurrent generated by using *p*-BQ as the electron scavenger (**Figure S5 and S6**). This result suggested that there is a considerable interfacial electron-hole recombination loss at the $BiVO_4$/Ag junction. Thus, we deposited Pt nanoparticles first and then Ag on top of Pt, so that Pt can efficiently collect photoexcited electrons from the Ca-doped $BiVO_4$/Pt interface and then transfer them to Ag for H_2O_2 production. When Pt alone was used, the photocurrent increased compared to the case of Ag, but its photocurrent was mostly associated with 4-electron PORR (**Figure S5 and S6**).

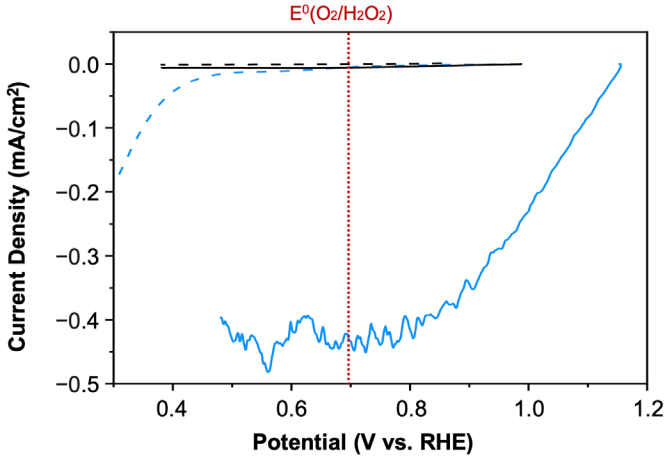

Figure 5. *J–V* plots of bare (black) and Pt/Ag-deposited (blue) Ca-doped $BiVO_4$ electrodes obtained in an O_2 saturated 0.5 M K_2SO_4 solution (pH 3). Solid lines were acquired under AM 1.5G illumination (100 mW/cm^2) and dotted lines were acquired in the dark. In order to help mass transport of O_2, stirring and O_2 purging were used during the *J–V* measurements. The photocurrent fluctuation shown in the blue solid line when the current density is high (~ –0.4 mA/cm^2) is due to the fluctuation of O_2 flux to the photoelectrode surface by stirring and O_2 purging.

The deposition of Pt/Ag on Ca-doped $BiVO_4$ in this study was achieved photoelectrochemically (**Figure 6a**). The reduction potentials of Ag^+ to Ag^0 (0.8 vs. NHE) and $[PtCl_4]^{2-}$ to Pt^0 (0.758 vs. NHE) are located inside the bandgap of $BiVO_4$.[51] Thus, photoexcited electrons in the CB of Ca-doped $BiVO_4$ can be utilized to reduce Ag^+ and $[PtCl_4]^2$ ions to Pt and Ag metal catalysts, respectively, on the surface of Ca-doped $BiVO_4$ at locations where electrons are readily available. The SEM image shows the size and distribution of Pt/Ag nanoparticle catalysts on Ca-doped $BiVO_4$ (**Figure 6b**). The metallic particles with around 50 nm diameters are uniformly distributed on the photocathode surface. The elemental mappings of the STEM image show that Ag is deposited mostly on top of Pt (**Figure 6c–e**), suggesting that Pt efficiently collects

photoexcited electrons and serves as an electron reservoir for Ag deposition. The XPS result confirming the presence of Pt and Ag on the Ca-doped $BiVO_4$/Pt/Ag sample is shown in **Figure S7.**

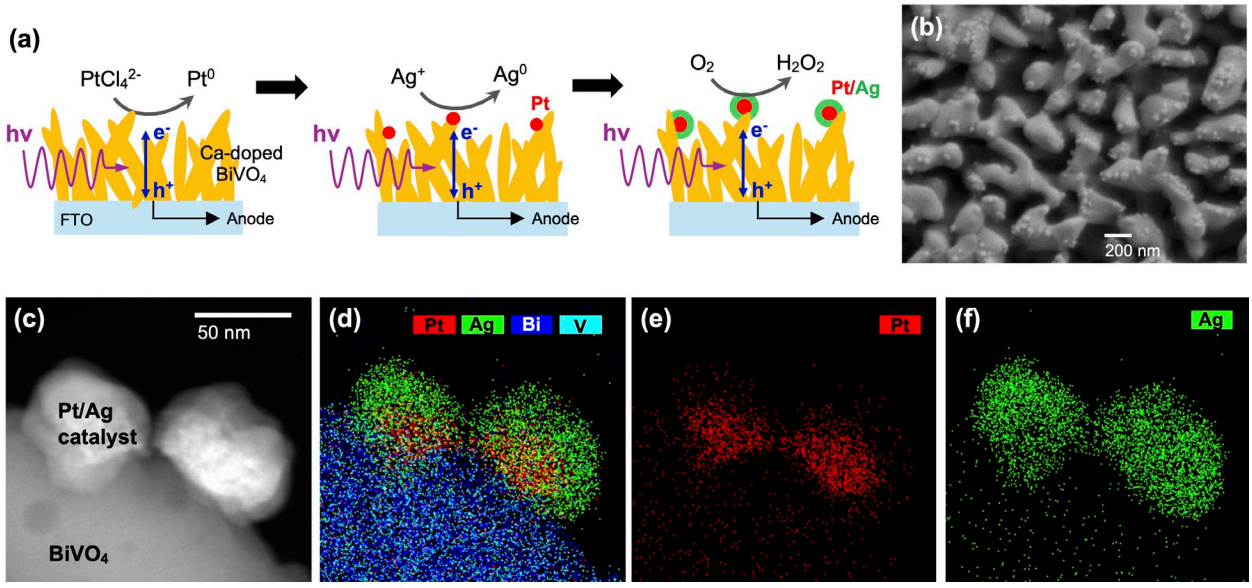

Figure 6. (a) Schematic illustration of the photoelectrodeposition of Pt/Ag particles on Ca-doped $BiVO_4$ photocathodes and photoelectrochemical H_2O_2 production. (b) SEM image of catalyst deposited Ca-doped $BiVO_4$. (c) HADDF-STEM image and (d–f) corresponding energy-dispersive X-ray spectroscopy (EDS) elemental mapping images focusing on Pt/Ag catalysts on $BiVO_4$.

After depositing Pt/Ag catalysts, the photocurrent for O_2 reduction by Ca-doped $BiVO_4$ was enhanced significantly compared to bare Ca-doped $BiVO_4$ and Ca-doped $BiVO_4$/Ag (**Figure 5 and S5**). In order to quantitatively analyze the amount of H_2O_2 produced, PORR was conducted at the constant potential of 0.8 V vs. RHE using four different Ca-doped $BiVO_4$/Pt/Ag samples, and the amount of produced H_2O_2 was quantified by iodometry. The results show that the average FE for H_2O_2 production is 45.8±7.8% at pH 2 and 35.1±1.4% at pH 3 (**Figure S6**). While the FE at pH 3 is slightly lower, we chose pH 3 as the optimal condition to use Ca-doped $BiVO_4$ for H_2O_2 production because at pH 2 $BiVO_4$ does not appear to have long-term stability (**Figure S8**).

We note that the FE obtained with Ca-doped $BiVO_4$/Ag/Pt is lower than that obtained with $BiVO_4$/Ag. This is because some Pt particles in Ca-doped $BiVO_4$/Ag/Pt were not covered by Ag and the uncovered Pt consumed photoexcited electrons mainly for 4-electron PORR. However, since the photocurrent generated by Ca-doped $BiVO_4$/Pt/Ag is much higher than that by Ca-doped $BiVO_4$/Ag, the rate of H_2O_2 production is higher with Ca-doped $BiVO_4$/Pt/Ag (**Figure S5 and S6**). For O_2 reduction where the only competing reaction is 4-electron O_2 reduction to H_2O that does not affect the purity of H_2O_2 produced, achieving a higher production rate of H_2O_2 is more important than achieving a higher FE for H_2O_2 production. We believe that further optimizations of the electrocatalysts and their interfaces with Ca-doped $BiVO_4$ can increase both the FE and production rates of H_2O_2.

The photoelectrochemical stability of Ca-doped $BiVO_4$/Pt/Ag was tested by performing PORR at 0.8 V vs. RHE for 10 hours, and a representative *J–t* plot generating a stable photocurrent

of around –0.4 mA/cm^2 is shown in **Figure 7a**. The XRD patterns and SEM images measured after the 10-h long *J–t* measurement confirmed that Ca-doped $BiVO_4$ is photoelectrochemically stable under this PORR condition (**Figure 7b and c)**. We note that for Cu-based photocathodes, this level of photostability is difficult to achieve without adding a protection layer between the photocathode and the catalyst.[5]

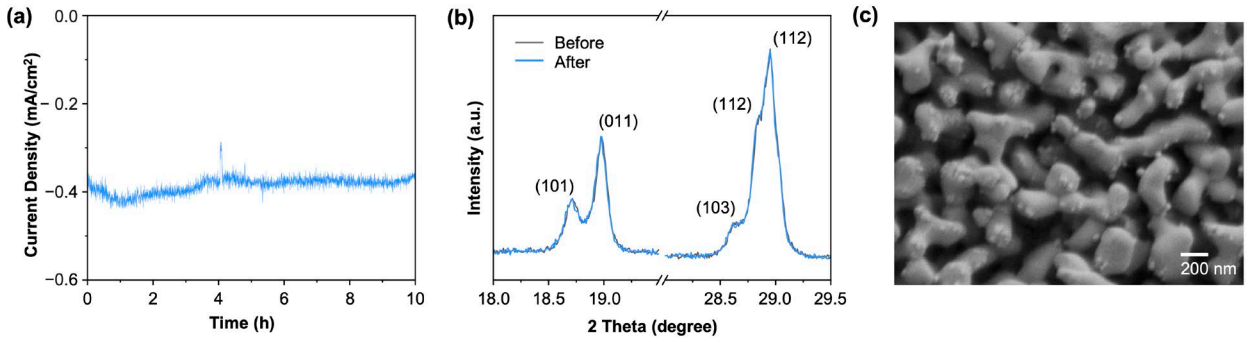

Figure 7. (a) *J–t* plot of Ca-doped $BiVO_4$/Pt/Ag at 0.8 V vs. RHE in an O_2 saturated 0.5 M potassium sulfate solution (pH 3) under AM 1.5G illumination (100 mW/cm^2). (b) XRD patterns of Ca-doped $BiVO_4$ before (grey) and after (blue) the 10-h electrolysis. (c) SEM image of Ca-doped $BiVO_4$ after the 10-h electrolysis.

In **Figure 5**, we compared the *J–V* plot of $BiVO_4$/Pt/Ag for PORR under illumination with that for EORR in the dark. The photocurrent onset for PORR is as early as 1.15 V vs. RHE. However, the onset potential for EORR is significantly more negative than the standard reduction potential of 2-electron ORR (0.695V vs. NHE).[51] This is because O_2 reduction kinetics in acidic solutions is slow and a considerable overpotential is required to initiate O_2 reduction even with the catalyst.

In contrast, when O_2 reduction was performed under illumination, the photoexcited electrons at the CBM (~0 V vs. RHE) of Ca-doped $BiVO_4$ have sufficient overpotential for O_2 reduction to H_2O_2. Thus, when a potential less positive than the flatband potential is applied to separate photogenerated electron-hole pairs, electrons reaching the catalyst can initiate photocurrent for O_2 reduction. As a result, the use of a photocathode having a very positive flatband potential such Ca-doped $BiVO_4$ can considerably decrease the potential input needed for H_2O_2 production. For instance, in order to generate –0.1 mA cm^{-2} for O_2 reduction, 0.35 V vs. RHE was needed in the dark while 1.09 V vs. RHE was needed under illumination with Ca-doped $BiVO_4$/Pt/Ag, saving 0.74 V (**Figure 5**).

Computational investigations of p-type $BiVO_4$. The first computational study on p-type *ms*-$BiVO_4$ was performed by Yan and co-workers, and they predicted a few dopants that can serve as shallow acceptors.[16] However, their work did not investigate hole polarons that may form in the resulting p-type *ms*-$BiVO_4$. Hole polarons in *ms*-$BiVO_4$ have been investigated by several other groups, however, these studies examined hole polarons formed by removing an electron from the *ms*-$BiVO_4$ system, and they did not investigate hole polarons formed by acceptor dopants incorporated into *ms*-$BiVO_4$.[52–54] Furthermore, the properties of the hole polaron, including its spatial distribution and the energy of the Kohn-Sham (KS) defect level (i.e., the defect level obtained from a DFT band-structure calculation), differ significantly in these studies. For example,

both Wiktor et al.[53] (using a supercell of size 10.30 × 10.26 × 23.50 Å and a PBE0-like functional with the Hartree-Fock mixing parameter $\alpha = 0.22$) and Liu et al.[54] (using a supercell of size 10.39 × 10.19 × 11.70 Å and the HSE functional with $\alpha = 0.25$) reported that the hole polaron is localized on one bismuth atom and its surrounding eight oxygen atoms; however these two studies report different KS defect levels (0.78 eV and 1 eV above the VBM, respectively). In contrast, Kweon et al.[52] (using the same functional as Liu et al., and a supercell of size 10.37 × 10.15 × 11.71 Å) found the hole polaron to be spread widely over adjacent Bi-O layers, with the KS defect level ~0.1 eV above the valence band edge. While the KS defect levels do not correspond to any experimental observable, they do qualitatively correlate with the extent of localization of the defect state, with KS defect levels closer to the valence band edge usually representing more delocalized holes (closer to the conduction band edge for more delocalized electrons). These inconsistencies in the position of the KS level and localization of the hole polaron in *ms*-$BiVO_4$ may be due to the different exchange-correlation functionals, k-meshes, and/or the supercell sizes used in the different calculations. We note that the supercell lattice parameter along the *c*-axis is ~11 Å in the studies by Liu et al.[54] and Kweon et al.[52] This size is comparable to the lattice parameter of a single unit cell of *ms*-$BiVO_4$ and it may not be sufficiently large to accurately characterize the hole polaron.

From the previous studies summarized above, we recognize that using hybrid exchange-correlation functionals and large supercell sizes is required to model the hole polaron in $BiVO_4$. Furthermore, as hole polarons resulting from acceptor dopants like Ca in $BiVO_4$ have not yet been investigated, such a study is critically needed to better understand experimental results obtained from p-type Ca-doped $BiVO_4$. In this study, we used a 4 × 4 × 2 supercell (768 atoms) and the dielectric dependent hybrid functional, as mentioned in the Methods section, with $\alpha = \varepsilon_\infty^{-1}$, where ε_∞ was determined from density functional perturbation theory. We note that the structural and electronic properties (e.g., lattice constants, dielectric constants, band gaps) of a broad range of materials calculated using the DDH functional (including n-type $BiVO_4$[55,56]) have shown excellent agreement with those obtained from experimental measurements, and this functional has been used to elucidate the mechanism of the enhanced charge transport in nitrogen-doped $BiVO_4$,[30,55] and to compare computed $BiVO_4$ band alignments with experiments.[56] As discussed in detail below, the computational results we obtained by modeling the hole polaron and acceptor dopants using large supercell sizes and the DDH exchange-correlation functional agree well with previously reported experimental results, such as hole absorption levels measured via transient absorption spectroscopy[57,58] and hole mobility trends observed via time-resolved terahertz spectroscopy[59] and kinetic modeling.[57]

Formation of hole polarons. The hole polaron in $BiVO_4$ was first created by removing an electron from the pristine supercell and choosing initial conditions for the total energy minimization where the Bi-O bonds were slightly contracted around a chosen Bi site. We then fully optimized the atomic positions in the supercell. **Figure 8a and b** present an iso-surface of the charge density of the hole polaron, where we see that the hole localizes on the bismuth atom with the initially contracted Bi-O bonds and its neighboring oxygen atoms; thus, the hole polaron has mostly Bi 6*s* and O 2*p* character. This charge localization causes the average length of the Bi-O bond to shorten from 2.47 Å to 2.42 Å. The charge distribution profile and bond length contraction found upon completion of the optimization of the atomic coordinates are consistent with those reported in previous hybrid DFT studies of the hole polaron in $BiVO_4$[53,54] which used PBE0 with $\alpha = 0.22$[53] and HSE with $\alpha = 0.25$[54] and smaller supercells. For example, we find a

contraction of 0.05 Å, comparable to those of 0.06 Å and 0.04 Å, reported by Wiktor et al.[53] and Liu et al.[54], respectively. We find a KS defect level of 0.57 eV above the valence band edge, which is lower than the values reported in previous studies[53,54] and suggests a more diffuse hole polaron state. We note that compared to the electron polaron in n-type $BiVO_4$,[55] the hole polaron in p-type $BiVO_4$ appears to be much more diffuse.

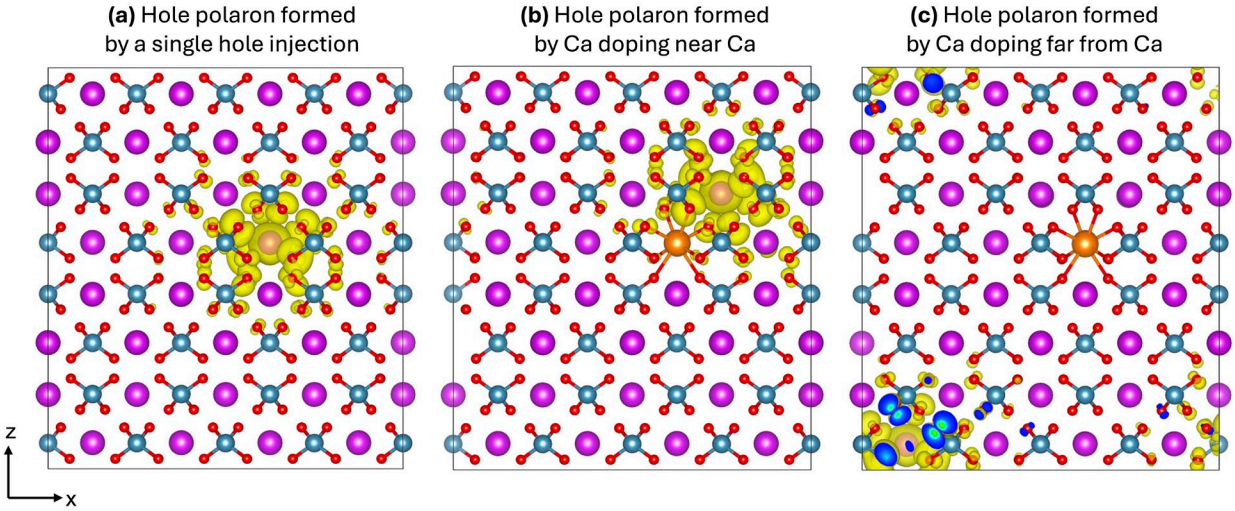

Figure 8. Iso-surfaces of the charge density of (a) the hole polaron formed by introducing one extra hole to $BiVO_4$, (b) the hole polaron formed by Ca doping at the Bi site nearest-neighbor (~4 Å) to the Ca dopant, and (c) the hole polaron formed by Ca doping at the Bi site farthest away (~19 Å) from the Ca dopant. Purple, blue, red, and orange spheres denote Bi, V, O, and Ca atoms (Isosurface level: 2.5 x 10^{-4} electrons/Å^3).

The polaron self-trapping energy ($E_{self-trap}$) calculated using Eq. 5 is –0.1 eV. The negative value shows that localization of the hole is favorable over delocalization of the carrier in the valence band, i.e., the hole polaron is thermodynamically more stable than a free carrier in the valence band. $E_{self-trap}$ is also referred to as the polaron binding energy. Note that the magnitude of $E_{self-trap}$ determines the free (not bound to any defect) hole polaron level with reference to the VBM. The free hole polaron level can also be calculated as the energy difference between the total energy of the perfect supercell (q = 0) and the supercell with the localized hole polaron (q = +1), with reference to the VBM. Thus, the free hole polaron level is equal to the (+1/0) charge-state transition level (CTL) of the hole polaron (**Figure 9a**).

Figure 9. Scheme showing (a) the free hole polaron level and (b) charge-state transition level (CTL) of Ca_{Bi} (0/-) relative to the free polaron level and VBM. (-x: polaron self-trapping energy or polaron binding energy, y: ionization energy of the Ca defect vs. VBM, z: ionization energy of the Ca defect vs. the free hole polaron level)

Following the work by Janotti et al.[36] and Sun et al.[35], we decompose $E_{self-trap}$ into the lattice strain energy $E_{lattice}$ and electronic energy $E_{electronic}$ contribution as shown in Eq. 6.

$$E_{self-trap} = E_{lattice} + E_{electronic} \quad (6)$$

$E_{lattice}$ is the energy penalty required to locally deform the lattice to accommodate the polaron and is calculated as the difference between the total energy of the supercell with the atomic positions corresponding to those of the polaronic state but without the hole (neutral supercell), and the total energy of the supercell of the pristine bulk. We find $E_{lattice}$ = 0.25 eV and, using Eq. 6, we obtain $E_{electronic}$ = −0.35 eV. $E_{electronic}$ is the energy difference between the localized hole polaron and a delocalized hole in the valence band, at atomic positions fixed to those of the hole polaron; it corresponds to the energy gained by localizing the hole via electron-phonon interaction.[60] Since the electronic energy gain $E_{electronic}$ exceeds the strain energy penalty $E_{lattice}$ required to distort the lattice, the polaronic state is stable. The magnitude of $E_{electronic}$ corresponds to the optical, vertical ionization energy required for a charge transition from the localized hole state in the bandgap to the delocalized valence band maximum and can be compared to experimentally determined values. We note that transient absorption spectroscopy experiments[57,58] measure a hole absorption level at 0.2–0.3 eV with respect to the VBM, which is comparable to the results for $E_{electronic}$ found here ($|E_{electronic}|$ = 0.35 eV). For a visual description of $E_{self-trap}$, $E_{lattice}$, and $E_{electronic}$, see **Figure S9**.

While a fraction of holes may exist as hole polarons due to the negative self-trapping energy, the value found here, –0.1 eV, is low enough for a fraction of holes to serve as delocalized carriers in the valence band at finite temperature. Indeed, when taking into account vibronic effects, the magnitudes of $E_{self-trap}$, $E_{electronic}$, and the activation energy for a hole polaron to become a delocalized free carrier in the valence band may even decrease further at finite temperature. We also note that hole trapping and de-trapping rate constants obtained from transient absorption spectroscopy-based kinetic models[57] are nearly equal, indicating a dynamic equilibrium of free holes and hole polarons in $BiVO_4$, consistent with the low value of $E_{self-trap}$ found in our study. The low value of $E_{self-trap}$ may also explain the different values of the hole mobility in $BiVO_4$ found in different experiments. For example, transient absorption spectroscopy studies at ambient conditions on undoped thin film *ms*-$BiVO_4$ report a hole mobility of 0.85 $cm^2\ V^{-1}\ s^{-1}$ (corresponding to free holes in the valence band), measured at 0.43 ps after excitation.[57] On the other hand, terahertz spectroscopy studies on undoped thin film *ms*-$BiVO_4$ in ambient conditions report mobilities of 0.02 $cm^2\ V^{-1}\ s^{-1}$ (corresponding to the presence of hole polarons), as measured at 100 ps after excitation.[61] Our computed low value of $E_{self-trap}$ explains these conflicting results by suggesting that a dynamic equilibrium between polarons and free carriers may exist and that their relative concentration may vary as a function of time after the excitation.

In our discussion above we considered a single hole polaron in a 4 × 4 × 2 supercell, which corresponds to a concentration of 10^{16} cm^{-3}, and was found to be localized. We also investigated

a higher hole concentration of ~10^{20} cm^{-3} by decreasing the supercell size (to 3 × 3 × 1 and 2 × 2 × 1). In this case, we found the hole polaron to be delocalized. This suggests that at concentrations higher than 10^{16} cm^{-3}, hole polarons in *ms*-$BiVO_4$ may be delocalized, which could have implications for p-type conductivity in this material. Interestingly, Butler et al.[59] estimated that at concentrations above 2 × 10^{16} cm^{-3}, hole polarons may achieve band-like mobility, and measured hole mobilities on the order 200 cm^2 V^{-1} s^{-1} for carrier concentrations of 10^{17} cm^{-3}. Our results as a function of concentration are consistent with these experimental findings. Note that previous first-principles studies with hole concentrations of 10^{20} cm^{-3} in $BiVO_4$[52–54] do not report hole delocalization. We emphasize that in our study we could observe such a difference in localization as a function of hole concentration due to the chosen hybrid functional and a sufficiently large supercell.

Ca dopant as a shallow acceptor. Calcium predominantly exists in the 2+ charge state, and therefore can function as an acceptor on both the Bi^{3+} and V^{5+} sites. However, previous first-principles studies on Ca doping in $BiVO_4$ report that Ca doping on the Bi site is likely more favorable due to lower formation energies compared to Ca doping on the V site.[16] This result is reasonable, considering the similar ionic radii and coordination preferences of Ca^{2+} and Bi^{3+} mentioned in the experimental section. Thus, a Ca dopant at the Bi site is the type of doping we investigated in our calculations.

In the following, we denote a Ca dopant at the Bi site as $(Ca_{Bi})^q$, where q is the charge state of the defect in the supercell. We consider two different scenarios: (a) Ca replacing Bi in the absence of any additional charge in the supercell (corresponding to the unionized acceptor) and (b) Ca replacing Bi in the presence of an extra electron in the supercell (corresponding to the ionized acceptor). Considering these two scenarios enables us to examine the stability of the various charge states of the Ca dopant in $BiVO_4$ as a function of the Fermi level and to determine the transition levels between different charge states.

The oxidation state of Ca is 2+, as forming Ca^{3+} requires very high ionization energies. Thus, in case (a) (neutral supercell), Ca^{2+} doping at a Bi^{3+} site bears a negative charge, and we denote the dopant as $(Ca_{Bi})^-$. To maintain neutrality, a compensating hole will be created in the supercell. This hole can form a delocalized state loosely bound to the $(Ca_{Bi})^-$ site via Coulomb attraction (resulting in $(Ca_{Bi})^0$) or a hole polaron next to the Ca dopant (resulting in a $[(Ca_{Bi})^-$—hole polaron$]^0$ defect complex). These situations correspond to an acceptor which is not ionized.

In case (b) (charged supercell), an electron is introduced to the supercell to annihilate the hole produced by Ca doping. This is to model $(Ca_{Bi})^-$ as an ionized acceptor. Such charged supercell calculations include a compensating jellium background charge to prevent divergence of the electrostatic energy of the system.

In the scenario (a) described above (neutral supercell), we found that the hole loosely bound to the $(Ca_{Bi})^-$ core is not delocalized; rather it forms a polaron on the Bi atom nearest neighbor to the Ca dopant (and extending to the oxygen atoms around the Bi site), as shown in **Figure 8b**. Thus a $[(Ca_{Bi})^-$—hole polaron$]^0$ defect complex is formed. The formation energy of such complex under oxygen-rich conditions, which mimics the experimental condition where Ca-doped $BiVO_4$ was prepared with O_2, is rather low (~0.16 eV), indicating a favorable Ca incorporation on the Bi site. Under oxygen-poor conditions, the formation energy increases (**Figure S10**). For all cases, the formation energy of the ionized acceptor $(Ca_{Bi})^-$ decreases further as the Fermi level increases above the VBM.

To determine if the Ca dopant is a shallow acceptor, we compute the thermodynamic charge-state transition level (CTL) between the unionized acceptor ($[(Ca_{Bi})^{-}-\text{hole polaron}]^{0}$ complex) and the ionized acceptor $(Ca_{Bi})^{-}$. This level is defined as the Fermi level (with respect to the VBM) at which the formation energies of the $[(Ca_{Bi})^{-}-\text{hole polaron}]^{0}$ complex and $(Ca_{Bi})^{-}$ are equal and the corresponding energy is also referred to as the thermal ionization energy of the acceptor required to create a delocalized free carrier in the valence band. We find that the Ca_{Bi} (0/–) CTL is 0.13 eV above the VBM and only 30 meV above the free hole polaron level (**Figure 9b**).

We note that the shallowness of the acceptor for a polaronic oxide is determined not by the thermal ionization energy with respect to VBM but by that with relative to the free hole polaron level. This is because once the hole polaron becomes a free hole polaron, unbound to the defect, it can serve as a charge carrier without being delocalized in the VB. This means that Ca_{Bi} with its thermal ionization energy as small as 30 meV with respect to the free hole polaron level is a shallow acceptor dopant in $BiVO_4$, which can be ionized at room temperature and generate free hole polarons contributing to p-type conductivity.

We also investigated an additional geometrical arrangement. Specifically, we optimized the geometry of the Ca-doped $BiVO_4$ system starting from initial conditions where Bi-O bonds farthest away from the Ca dopant (~19 Å) were contracted. We found that the polaron localizes on the initially perturbed Bi site (and the O atoms around that site), as shown in **Figure 8c**. The energy of this geometrical arrangement is only 25 meV higher than that of the structure with the hole polaron localized next to the Ca dopant (**Figure 8b**). This energy difference corresponds to the energy required to extract the hole from the $[(Ca_{Bi})^{-}-\text{hole polaron}]^{0}$ defect complex into the bulk region of $BiVO_4$, where it can act as a free hole polaron, and this value agrees well with the energy difference between the Ca_{Bi} (0/–) CTL and the free hole polaron level (30 meV). In the two cases considered here (corresponding to **Figure 8b and c**), the KS defect levels introduced by the Ca dopant in $BiVO_4$ are around 0.6 eV above the VBM, a value nearly equal to the KS defect level of the hole polaron in pristine $BiVO_4$ (0.57 eV), indicating that the presence of Ca has no influence on the position of the hole polaron KS defect level.

We emphasize here that doping $BiVO_4$ with an acceptor will always result in the formation of hole polarons, instead of delocalized holes, at low temperature. (Some of these hole polarons may become free carriers in the valence band and exhibit band-like mobility at higher temperature). This is a consequence of the intrinsic self-trapping energy ($E_{self-trap}$) of hole polarons in $BiVO_4$ (–0.1 eV). The CTL of any acceptor dopant in $BiVO_4$ is not expected to be lower than 0.1 eV because any delocalized hole introduced by the ionization of the acceptor dopant will be self-trapped to form a polaron with a polaron binding energy of 0.1 eV. Hence the acceptor dopant (0/–) CTL will be at least 0.1 eV above the VBM. Thus, the fact that the Ca_{Bi} (0/–) CTL (0.13 eV) is very close to 0.1 eV suggests that Ca_{Bi} is likely one of the shallowest acceptors that can make p-type *ms*-$BiVO_4$.

Conclusions

In summary, we have demonstrated the synthesis of p-type *ms*-$BiVO_4$ via atomic doping of Ca^{2+} at the Bi^{3+} site under the O_2-rich environment. The use of the O_2-rich environment was found to be critical for incorporating more Ca acceptor dopants by lowering the formation energy of Ca_{Bi} and for decreasing the concentration of oxygen vacancies that serve as donor-type defects.

The photoelectrochemical property of Ca-doped *ms*-$BiVO_4$ was evaluated using *p*-BQ as an electron scavenger, which revealed that the flatband potential of our Ca-doped *ms*-$BiVO_4$ is ≥ 1.0 V vs. RHE and that the IPCE of Ca-doped *ms*-$BiVO_4$ at 0.65 V vs. RHE is ~20% for photons with wavelengths shorter than 460 nm. Benefiting from the chemical stability of *ms*-$BiVO_4$, we also demonstrated the possibility of using a Ca-doped *ms*-$BiVO_4$ photocathode coupled with Ag and Pt/Ag catalysts for 2-electron PORR to H_2O_2 in mildly acidic solutions. Our computational investigations using hybrid density functional theory revealed that holes in *ms*-$BiVO_4$ form polarons with a self-trapping energy of −0.1 eV. This low self-trapping energy may result in free carriers in the valence band and therefore band-like mobility at finite temperatures. Our simulations also demonstrated that Ca is an effective shallow acceptor dopant in *ms*-$BiVO_4$ due to its low formation energy and low thermal ionization energy of 30 meV above the free polaron level, thereby resulting in its p-type behavior. Together, our experimental and computational findings provide important insights into designing *ms*-$BiVO_4$, a conventional n-type material, as a p-type material, enabling the use of *ms*-$BiVO_4$ as a photocathode.

ASSOCIATED CONTENT

Supporting Information

The Supporting Information is available free of charge on the ACS Publication website: additional characterization of Ca-doped $BiVO_4$ and Ca-doped $BiVO_4$/Pt/Ag, Comparison of Ca-doped $BiVO_4$/Ag Ca-doped $BiVO_4$/Pt and Ca-doped $BiVO_4$/Pt/Ag for solar H_2O_2 production, UV−vis spectra used for H_2O_2 quantification, a scheme showing the relationship of $E_{self-trap}$, $E_{lattice}$, and $E_{electronic}$, and defect formation energy of Ca_{Bi} with various oxygen chemical potentials (PDF).

AUTHOR INFORMATION

Corresponding Author

*Email: kschoi@chem.wisc.edu
*Email: gagalli@uchicago.edu

Notes

The authors declare no competing interests.

Acknowledgements

The experimental work was supported by the Division of Chemical Sciences, Geosciences, and Biosciences, Office of Basic Energy Sciences of the U.S. Department of Energy through Grant DE-SC0024211. The computational work was supported by the National Science Foundation (NSF) through Grant CHE-2350199. V.S. was supported by the Maria Goeppert Mayer Named Fellowship, under the Laboratory Directed Research and Development (LDRD) funding from Argonne National Laboratory, provided by the Director of the Office of Science of the U.S. Department of Energy under Contract No. DE-AC02-06CH11357. This research used Materials

Synthesis & Characterization and Proximal Probes facilities of the Center for Functional Nanomaterials, which is a U.S. DOE Office of Science Facility, at Brookhaven National Laboratory under Contract No. DE-SC0012704. This research used computational resources of the National Energy Research Scientific Computing Center (NERSC), a Department of Energy Office of Science User Facility using NERSC award DDRERCAP0029604.

References

(1) Tian, C.; Dorakhan, R.; Wicks, J.; Chen, Z.; Choi, K. S.; Singh, N.; Schaidle, J. A.; Holewinski, A.; Vojvodic, A.; Vlachos, D. G.; Broadbelt, L. J.; Sargent, E. H. Progress and Roadmap for Electro-Privileged Transformations of Bio-Derived Molecules. *Nat. Catal.* **2024**, *7* (4), 350–360. DOI: 10.1038/s41929-024-01131-6

(2) Walter, M. G.; Warren, E.; McKone Jr.; Boettcher, S.; Mi, Q.; Santori, E.; Lewis, N. Solar Water Splitting Cells. *Chem. Rev.* **2010**, *110* (11), 6446–6473. DOI: 10.1021/cr1002326

(3) Sivula, K.; van de Krol, R. Semiconducting Materials for Photoelectrochemical Energy Conversion. *Nat. Rev. Mater.* **2016**, *1* (2), 15010. DOI: 10.1038/natrevmats.2015.10

(4) Lee, D. K.; Lee, D.; Lumley, M. A.; Choi, K.; Lee, D. K. Progress on Ternary Oxide-Based Photoanodes for Use in Photoelectrochemical Cells for Solar Water Splitting. *Chem. Soc. Rev.* **2019**, *48*, 2126. DOI: 10.1039/c8cs00761f

(5) Lumley, M. A.; Radmilovic, A.; Jang, Y. J.; Lindberg, A. E.; Choi, K. S. Perspectives on the Development of Oxide-Based Photocathodes for Solar Fuel Production. *J. Am. Chem. Soc.* **2019**, *141* (46), 18358–18369. DOI: 10.1021/jacs.9b07976

(6) Pan, L.; Kim, J. H.; Mayer, M. T.; Son, M.; Ummadisingu, A.; Lee, J. S.; Hagfeldt, A.; Luo, J.; Grätzel, M. Boosting the Performance of Cu_2O Photocathodes for Unassisted Solar Water Splitting Devices. *Nat. Catal.* **2018**, *1*, 412–420. DOI: 10.1038/s41929-018-0077-6

(7) Wheeler, G. P.; Choi, K. S. Photoelectrochemical Properties and Stability of Nanoporous P-Type $LaFeO_3$ Photoelectrodes Prepared by Electrodeposition. *ACS Energy Lett.* **2017**, *2* (10), 2378–2382. DOI: 10.1021/acsenergylett.7b00642

(8) Wheeler, G. P.; Choi, K. S. Investigation of P-Type $Ca_2Fe_2O_5$ as a Photocathode for Use in a Water Splitting Photoelectrochemical Cell. *ACS Appl. Energy Mater.* **2018**, *1* (9), 4917–4923. DOI: 10.1021/acsaem.8b00934

(9) Wheeler, G. P.; Baltazar, V. U.; Smart, T. J.; Radmilovic, A.; Ping, Y.; Choi, K. S. Combined Theoretical and Experimental Investigations of Atomic Doping to Enhance Photon Absorption and Carrier Transport of $LaFeO_3$ Photocathodes. *Chem. Mater.* **2019**, *31* (15), 5890–5899. DOI: 10.1021/acs.chemmater.9b02141

(10) Seo, D.; Grieder, A.; Radmilovic, A.; Alamudun, S. F.; Yuan, X.; Ping, Y.; Choi, K. Atomic Doping to Enhance the P-Type Behavior of $BiFeO_3$ Photoelectrodes for Solar H_2O_2 Production. *J. Mater. Chem. A* **2024**, *12*, 20437-20448. DOI: 10.1039/d4ta03191a

(11) Kim, T. W.; Choi, K.-S. Nanoporous $BiVO_4$ Photoanodes with Dual-Layer Oxygen Evolution Catalysts for Solar Water Splitting. *Science* **2014**, *343* (6174), 990–994. DOI: 10.1126/science.1246913

(12) Lee, D. K.; Choi, K. S. Enhancing Long-Term Photostability of $BiVO_4$ Photoanodes for Solar Water Splitting by Tuning Electrolyte Composition. *Nat. Energy* **2018**, *3* (1), 53–60. DOI: 10.1038/s41560-017-0057-0

(13) Kuang, Y.; Jia, Q.; Ma, G.; Hisatomi, T.; Minegishi, T.; Nishiyama, H.; Nakabayashi, M.; Shibata, N.; Yamada, T.; Kudo, A.; Domen, K. Ultrastable Low-Bias Water Splitting Photoanodes via Photocorrosion Inhibition and in Situ Catalyst Regeneration. *Nat. Energy* **2017**, *2* (1), 1–3. DOI: 10.1038/nenergy.2016.191

(14) Wang, J.; Song, Y.; Hu, J.; Li, Y.; Wang, Z.; Yang, P.; Wang, G.; Ma, Q.; Che, Q.; Dai, Y.; Huang, B. Photocatalytic Hydrogen Evolution on P-Type Tetragonal Zircon $BiVO_4$. *Appl. Catal. B Environ.* **2019**, *251*, 94–101. DOI: 10.1016/j.apcatb.2019.03.049

(15) Liang, X.; Wang, P.; Tong, F.; Liu, X.; Wang, C.; Wang, M.; Zhang, Q.; Wang, Z.; Liu, Y.; Zheng, Z.; Dai, Y.; Huang, B. Bias-Free Solar Water Splitting by Tetragonal Zircon $BiVO_4$ Nanocrystal Photocathode and Monoclinic Scheelite $BiVO_4$ Nanoporous Photoanode. *Adv. Funct. Mater.* **2021**, *31* (8), 2008656. DOI: 10.1002/adfm.202008656.
(16) Yin, W.; Wei, S.; Al-Jassim, M. M.; Turner, J.; Yan, Y. Doping Properties of Monoclinic $BiVO_4$ Studied by First-Principles Density-Functional Theory. *Phys. Rev. B* **2011**, *83* (15), 155102. DOI: 10.1103/PhysRevB.83.155102
(17) Abdi, F. F.; Starr, D. E.; Ahmet, I. Y.; van de Krol, R. Photocurrent Enhancement by Spontaneous Formation of a P-n Junction in Calcium-Doped Bismuth Vanadate Photoelectrodes. *Chempluschem* **2018**, *83* (10), 941–946. DOI: 10.1002/cplu.201800119
(18) Pylarinou, M.; Sakellis, E.; Tsipas, P.; Romanos, G. E.; Gardelis, S.; Dimoulas, A.; Likodimos, V. Opals for Photoelectrocatalytic Pharmaceutical Degradation under Visible Light. *ACS Appl. Nano Mater.* **2023**, *6* (8), 6759–6771. DOI: /10.1021/acsanm.3c00469
(19) Yang, S.; Verdaguer-Casadevall, A.; Arnarson, L.; Silvioli, L.; Čolić, V.; Frydendal, R.; Rossmeisl, J.; Chorkendorff, I.; Stephens, I. E. L. Toward the Decentralized Electrochemical Production of H_2O_2: A Focus on the Catalysis. *ACS Catal.* **2018**, *8* (5), 4064–4081. DOI: 10.1021/acscatal.8b00217
(20) Hohenberg, P.; Kohn, W. Inhomogeneous Electron Gas. *Phys. Rev.* **1964**, *136* (3B), B864–B871. DOI: 10.1103/PhysRev.136.B864
(21) Kohn, W.; Sham, L. J. Self-Consistent Equations Including Exchange and Correlation Effects. *Phys. Rev.* **1965**, *140* (4A), A1133–A1138. DOI: 10.1103/PhysRev.140.A1133
(22) Giannozzi, P.; Baroni, S.; Bonini, N.; Calandra, M.; Car, R.; Cavazzoni, C.; Ceresoli, D.; Chiarotti, G. L.; Cococcioni, M.; Dabo, I.; Corso, A. D.; Gironcoli, S. de; Fabris, S.; Fratesi, G.; Gebauer, R.; Gerstmann, U.; Gougoussis, C.; Kokalj, A.; Lazzeri, M.; Martin-Samos, L.; Marzari, N.; Mauri, F.; Mazzarello, R.; Paolini, S.; Pasquarello, A.; Paulatto, L.; Sbraccia, C.; Scandolo, S.; Sclauzero, G.; Seitsonen, A. P.; Smogunov, A.; Umari, P.; Wentzcovitch, R. M. QUANTUM ESPRESSO: A Modular and Open-Source Software Project for Quantum Simulations of Materials. *J. Phys.: Condens. Matter* **2009**, *21* (39), 395502. DOI: 10.1088/0953-8984/21/39/395502
(23) Giannozzi, P.; Andreussi, O.; Brumme, T.; Bunau, O.; Nardelli, M. B.; Calandra, M.; Car, R.; Cavazzoni, C.; Ceresoli, D.; Cococcioni, M.; Colonna, N.; Carnimeo, I.; Corso, A. D.; Gironcoli, S. de; Delugas, P.; DiStasio, R. A.; Ferretti, A.; Floris, A.; Fratesi, G.; Fugallo, G.; Gebauer, R.; Gerstmann, U.; Giustino, F.; Gorni, T.; Jia, J.; Kawamura, M.; Ko, H.-Y.; Kokalj, A.; Küçükbenli, E.; Lazzeri, M.; Marsili, M.; Marzari, N.; Mauri, F.; Nguyen, N. L.; Nguyen, H.-V.; Otero-de-la-Roza, A.; Paulatto, L.; Poncé, S.; Rocca, D.; Sabatini, R.; Santra, B.; Schlipf, M.; Seitsonen, A. P.; Smogunov, A.; Timrov, I.; Thonhauser, T.; Umari, P.; Vast, N.; Wu, X.; Baroni, S. Advanced Capabilities for Materials Modelling with Quantum ESPRESSO. *J. Phys.: Condens. Matter* **2017**, *29* (46), 465901. DOI: 10.1088/1361-648X/aa8f79
(24) Giannozzi, P.; Baseggio, O.; Bonfà, P.; Brunato, D.; Car, R.; Carnimeo, I.; Cavazzoni, C.; de Gironcoli, S.; Delugas, P.; Ferrari Ruffino, F.; Ferretti, A.; Marzari, N.; Timrov, I.; Urru, A.; Baroni, S. Quantum ESPRESSO toward the Exascale. *The Journal of Chemical Physics* **2020**, *152* (15), 154105. DOI: 10.1063/5.0005082
(25) Schlipf, M.; Gygi, F. Optimization Algorithm for the Generation of ONCV Pseudopotentials. *Computer Physics Communications* **2015**, *196*, 36–44. DOI: 10.1016/j.cpc.2015.05.011

(26) Hamann, D. R. Optimized Norm-Conserving Vanderbilt Pseudopotentials. *Phys. Rev. B* **2013**, *88* (8), 085117. DOI: 10.1103/PhysRevB.88.085117
(27) Zhang, Y.; Yang, W. A Challenge for Density Functionals: Self-Interaction Error Increases for Systems with a Noninteger Number of Electrons. *J. Chem. Phys.* **1998**, *109* (7), 2604–2608. DOI: 10.1063/1.476859
(28) Pacchioni, G.; Frigoli, F.; Ricci, D.; Weil, J. A. Theoretical Description of Hole Localization in a Quartz Al Center: The Importance of Exact Electron Exchange. *Phys. Rev. B* **2000**, *63* (5), 054102. DOI: 10.1103/physrevb.63.054102
(29) Lægsgaard, J.; Stokbro, K. Hole Trapping at Al Impurities in Silica: A Challenge for Density Functional Theories. *Phys. Rev. Lett.* **2001**, *86* (13), 2834–2837. DOI: 10.1103/PhysRevLett.86.2834
(30) Kim, T. W.; Ping, Y.; Galli, G. A.; Choi, K.-S. Simultaneous Enhancements in Photon Absorption and Charge Transport of Bismuth Vanadate Photoanodes for Solar Water Splitting. *Nat. Commun.* **2015**, *6* (1), 8769. DOI: 10.1038/ncomms9769
(31) Sleight, A. W.; Chen, H. -y.; Ferretti, A.; Cox, D. E. Crystal Growth and Structure of $BiVO_4$. *Mater. Res. Bull.* **1979**, *14* (12), 1571–1581. DOI: 10.1016/0025-5408(72)90227-9
(32) Wiktor, J.; Reshetnyak, I.; Ambrosio, F.; Pasquarello, A. Comprehensive Modeling of the Band Gap and Absorption Spectrum of $BiVO_4$. *Phys. Rev. Mater.* **2017**, *1* (2), 022401. DOI: 10.1103/PhysRevMaterials.1.022401
(33) Freysoldt, C.; Grabowski, B.; Hickel, T.; Neugebauer, J.; Kresse, G.; Janotti, A.; Van de Walle, C. G. First-Principles Calculations for Point Defects in Solids. *Rev. Mod. Phys.* **2014**, *86* (1), 253–305. DOI: 10.1103/RevModPhys.86.253
(34) Freysoldt, C.; Neugebauer, J.; Van De Walle, C. G. Fully *Ab Initio* Finite-Size Corrections for Charged-Defect Supercell Calculations. *Phys. Rev. Lett.* **2009**, *102* (1), 016402. DOI: 10.1103/PhysRevLett.102.016402
(35) Sun, L.; Huang, X.; Wang, L.; Janotti, A. Disentangling the Role of Small Polarons and Oxygen Vacancies in CeO_2. *Phys. Rev. B* **2017**, *95* (24), 245101. DOI: 10.1103/PhysRevB.95.245101
(36) Janotti, A.; Franchini, C.; Varley, J. B.; Kresse, G.; Van de Walle, C. G. Dual Behavior of Excess Electrons in Rutile TiO_2. *Phys. Status Solidi - Rapid Res. Lett.* **2013**, *7* (3), 199–203. DOI: 10.1002/pssr.201206464
(37) Shannon, R. D. Revised Effective Ionic Radii and Systematic Studies of Interatomie Distances in Halides and Chaleogenides. *Acta Cryst.* **1976**, *A32*, 751-767. DOI: 10.1107/S0567739476001551
(38) Tokunaga, S.; Kato, H.; Kudo, A. Selective Preparation of Monoclinic and Tetragonal $BiVO_4$ with Scheelite Structure and Their Photocatalytic Properties. *Chem. Mater.* **2001**, *13* (12), 4624–4628. DOI: 10.1021/cm0103390
(39) Park, Y.; Mc Donald, K. J.; Choi, K. S. Progress in Bismuth Vanadate Photoanodes for Use in Solar Water Oxidation. *Chem. Soc. Rev.* **2013**, *42* (6), 2321–2337. DOI: 10.1039/c2cs35260e
(40) Govindaraju, G. V.; Wheeler, G. P.; Lee, D.; Choi, K. S. Methods for Electrochemical Synthesis and Photoelectrochemical Characterization for Photoelectrodes. *Chem. Mater.* **2017**, *29* (1), 355–370. DOI: 10.1021/acs.chemmater.6b03469

(41) Wi, D. H.; Lumley, M. A.; Xi, Z.; Liu, M.; Choi, K. Investigation of Electron Extraction and Protection Layers on Cu_2O Photocathodes. *Chem. Mater.* **2023**, *35* (11), 4385–4392. DOI: 10.1021/acs.chemmater.3c00543
(42) Brillas, E.; Sire, I.; Oturan, M. A. Electro-Fenton Process and Related Electrochemical Technologies Based on Fenton's Reaction Chemistry. *Chem. Rev.* **2009**, *109* (12), 6570–6631. DOI: 10.1021/cr900136g
(43) Campos-martin, J. M.; Blanco-brieva, G.; Fierro, J. L. G. Hydrogen Peroxide Synthesis: An Outlook beyond the Anthraquinone Process. *Angew. Chem. Int. Ed.* **2006**, *45*, 6962–6984. DOI: 10.1002/anie.200503779
(44) Perry, S. C.; Vieira, L.; Sieber, V.; Wang, L.; León, C. P. De; Walsh, F. C. Electrochemical Synthesis of Hydrogen Peroxide from Water and Oxygen. *Nat. Rev. Chem.* **2019**, *3*, 442–458. DOI: 10.1038/s41570-019-0110-6
(45) Ko, M.; Lim, J. S.; Jang, J. W.; Joo, S. H. Bias-Free Photoelectrochemical H_2O_2 Production and Its In Situ Applications. *ACS ES T Eng.* **2023**, *3* (7), 910–922. DOI: 10.1021/acsestengg.3c00053
(46) Berl, E. A New Cathodic Process for the Production Of H_2O_2. *Trans. Electrochem. Soc.***1939**, *76*, 359. DOI: 10.1149/1.3500291
(47) Qiang, Z.; Chang, J. H.; Huang, C. P. Electrochemical Generation of Hydrogen Peroxide from Dissolved Oxygen in Acidic Solutions. *Water Res.* **2002**, *36* (1), 85–94. DOI: 10.1016/S0043-1354(01)00235-4
(48) Nicoll, W. D.; Smith, A. F. Stability of dilute alkaline solutions of hydrogen peroxide. *Ind. Eng. Chem.* **1955**, *47* (12), 2548–2554. DOI: 10.1021/ie50552a051
(49) Sheng, H.; Ross, R. D.; Schmidt, J. R.; Jin, S. Metal-Compound-Based Electrocatalysts for Hydrogen Peroxide Electrosynthesis and the Electro-Fenton Process. *ACS Energy Lett.* **2023**, *8* (1), 196–212. DOI: 10.1021/acsenergylett.2c01945
(50) Blizanac, B. B.; Ross, P. N.; Markovic, N. M. Oxygen Electroreduction on Ag(1 1 1): The pH Effect. *Electrochim. Acta* **2007**, *52* (6), 2264–2271. DOI: 10.1016/j.electacta.2006.06.047
(51) Bard, A. J.; Faulkner, L. R.; White, H. S. *Electrochemical Methods: Fundamentals and Applications*, 3rd ed.; John Wiley & Sons, 2022. DOI:
(52) Kweon, K. E.; Hwang, G. S. Structural Phase-Dependent Hole Localization and Transport in Bismuth Vanadate. *Phys. Rev. B* **2013**, *87* (20), 205202. DOI: 10.1103/PhysRevB.87.205202
(53) Wiktor, J.; Ambrosio, F.; Pasquarello, A. Role of Polarons in Water Splitting: The Case of $BiVO_4$. *ACS Energy Lett.* **2018**, *3* (7), 1693–1697. DOI: 10.1021/acsenergylett.8b00938
(54) Liu, T.; Cui, M.; Dupuis, M. Hole Polaron Transport in Bismuth Vanadate $BiVO_4$ from Hybrid Density Functional Theory. *J. Phys. Chem. C* **2020**, *124* (42), 23038–23044. DOI: 10.1021/acs.jpcc.0c07408
(55) Seo, H.; Ping, Y.; Galli, G. Role of Point Defects in Enhancing the Conductivity of $BiVO_4$. *Chem. Mater.* **2018**, *30* (21), 7793–7802. DOI: 10.1021/acs.chemmater.8b03201
(56) Wang, W.; Strohbeen, P. J.; Lee, D.; Zhou, C.; Kawasaki, J. K.; Choi, K.-S.; Liu, M.; Galli, G. The Role of Surface Oxygen Vacancies in $BiVO_4$. *Chem. Mater.* **2020**, *32* (7), 2899–2909. DOI: 10.1021/acs.chemmater.9b05047
(57) Cooper, J. K.; Reyes-Lillo, S. E.; Hess, L. H.; Jiang, C.-M.; Neaton, J. B.; Sharp, I. D. Physical Origins of the Transient Absorption Spectra and Dynamics in Thin-Film

Semiconductors: The Case of $BiVO_4$. *J. Phys. Chem. C* **2018**, *122* (36), 20642–20652. DOI: 10.1021/acs.jpcc.8b06645

(58) Ravensbergen, J.; Abdi, F. F.; van Santen, J. H.; Frese, R. N.; Dam, B.; van de Krol, R.; Kennis, J. T. M. Unraveling the Carrier Dynamics of $BiVO_4$: A Femtosecond to Microsecond Transient Absorption Study. *J. Phys. Chem. C* **2014**, *118* (48), 27793–27800. DOI: 10.1021/jp509930s

(59) T. Butler, K.; J. Dringoli, B.; Zhou, L.; M. Rao, P.; Walsh, A.; V. Titova, L. Ultrafast Carrier Dynamics in $BiVO_4$ Thin Film Photoanode Material: Interplay between Free Carriers, Trapped Carriers and Low-Frequency Lattice Vibrations. *Journal of Materials Chemistry A* **2016**, *4* (47), 18516–18523. DOI: 10.1039/c6ta07177e

(60) Franchini, C.; Reticcioli, M.; Setvin, M.; Diebold, U. Polarons in Materials. *Nat Rev Mater* **2021**, *6* (7), 560–586. DOI: 10.1038/s41578-021-00289-w

(61) Ziwritsch, M.; Müller, S.; Hempel, H.; Unold, T.; Abdi, F. F.; van de Krol, R.; Friedrich, D.; Eichberger, R. Direct Time-Resolved Observation of Carrier Trapping and Polaron Conductivity in $BiVO_4$. *ACS Energy Lett.* **2016**, *1* (5), 888–894. DOI: 10.1021/acsenergylett.6b00423

TOC Graphic

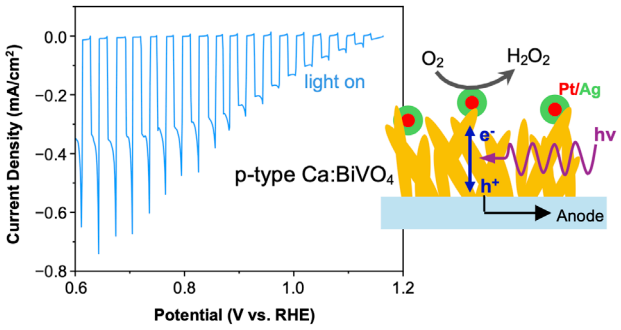
Current Density (mA/cm²)
0.0
−0.2
−0.4
−0.6
−0.8
0.6
0.8
1.0
1.2
Potential (V vs. RHE)
light on
p-type Ca:BiVO4
O2
H2O2
Pt/Ag
hv
e-
h+
Anode